

1

2

The Seasonal Cycle of Significant Wave Height in the Ocean: Local vs Remote Forcing

5

Luke V. Colosi¹, Ana B. Villas Bôas¹, Sarah T. Gille¹

6

¹Scripps Institution of Oceanography, La Jolla, California

7

Key Points:

8

- Identification of summer wind anomaly regions which correspond to hypothesized expansion fan wind regions.
 - Magnitude of significant wave height increase is determined by local conditions within summer wind anomaly region.
 - Summer wind anomaly regions have high tendency for wind-sea dominated wave fields during summer months implying deviation from SWH annual cycle occurs due to locally forced waves.

8

1

10

11

12

Corresponding author: Luke V. Colosi, lcolosi@ucsd.edu

15 **Abstract**

16 Significant wave height (SWH) provides insight into the interactions between the ocean
 17 and the atmosphere. In the Northern and Southern Hemispheres, wave heights typically
 18 undergo a sinusoidal annual cycle, with larger SWH in winter in response to seasonal changes
 19 in high-latitude storm patterns that generate equatorward propagating swell waves. In
 20 the California coastal region, local expansion fan wind events occur in boreal spring and
 21 summer, leading to local deviations from the expected hemispheric-scale annual cycle
 22 in SWH. Other coastal regions with early summer expansion fan wind events occur in
 23 locations with coastal topography and atmospheric forcing similar to California. These
 24 regions, here are designated as summer wind anomaly regions (SWARs). In this study
 25 intra-annual variability of surface gravity waves is analyzed globally using two decades
 26 of satellite-derived SWH and wind speed data. The dividing line between swell originat-
 27 ing in the Northern and Southern Hemispheres is slightly south of the equator and varies
 28 by location depending on a variety of factors, including topography and island shadow-
 29 ing effects. In SWARs, the fraction of wave variability attributed to local wind events
 30 varies depending on local conditions. Global maps of probability of swell based on wave
 31 age confirm that the wave-field in SWARs is typically dominated by locally forced waves
 32 during the spring and summer months. The phasing of the annual cycle is used to quan-
 33 titatively identify SWARs. Wave-field modulation by strong wind events may lead to en-
 34 hanced wave breaking which could have implications for air-sea fluxes.

35 **Plain Language Summary**

36 [enter your Plain Language Summary here or delete this section]

37 **1 Introduction**

38 Surface gravity waves are fundamental to ocean–atmosphere interactions, and they
 39 mediate exchanges of momentum, heat, gasses, and energy cavaleri2012wind,edson2007coupled,sullivan2004oceani-
 40 villasboas2019integrated. The flux of momentum from the wind to the wave field is the
 41 principal generation mechanism of surface waves ardhuin2015ocean, which are commonly
 42 defined as having wave periods between 1 to 30 seconds munk1951origin. These waves
 43 can propagate long distances across the oceans away from their generation site snodgrass1966propagation.
 44 Thus, the wave field in a particular location represents the superposition of locally forced

45 waves (“wind-sea”) and remotely forced waves (“swell”) sverdrup1947wind, semedo2011global,
46 jiang2013global, villas2017characterization.

47 Previous studies have used satellite data and models to analyze the climatology of
48 ocean winds and waves. young1999seasonal, for example, investigated global variations
49 in wave and wind conditions using significant wave height (SWH) and wind speed (WSP).
50 Results showed that wave and wind conditions vary geographically and seasonally. SWH
51 undergoes an annual cycle in response to seasonal variability of storm systems. stopa2019seasonality
52 further investigated global wind and wave seasonality by describing the seasonal char-
53 acteristics of SWH and WSP. The author concluded that each ocean basin experiences
54 seasonal patterns, with the Southern Hemisphere experiencing more active sea state than
55 the Northern Hemisphere. echevarria2019seasonal extended the young1999seasonal global
56 analysis using directional wave spectra from a WAVEWATCH III hindcast to analyze
57 intra-annual variability of the global wave field by exploring multiple wave modes gen-
58 erated from particular synoptic atmospheric forcings present in the wave field. While many
59 studies further explore the large-scale temporal trends and climate modes of the global
60 wind and wave fields (? , ? , e.g.,)]young2011global, stopa2014periodicity, others focus on
61 separating the wave field into swell and wind-sea components using remote sensing and
62 model data (? , ? , e.g.,)]jiang2013global, semedo2011global, zheng2016analysis. For ex-
63 ample, semedo2011global investigated the intra and interannual variability of spectrally
64 partitioned wind sea and swell SWH and showed that the global oceans are strongly dom-
65 inated by swell. Despite comprehensive global-scale studies, there is a lack of regional
66 analysis investigating the response of the sea state to regional-scale winds.

67 villas2017characterization analyzed how regional-scale wind variability can cause
68 deviations from the SWH seasonal cycle to arise in the temporal variability of SWH. The
69 authors explored a distinct deviation occurring in the California coast region due to a
70 local wind phenomena known as expansion fan winds which are generated by a combi-
71 nation of atmospheric conditions and coastal topography (Winant et al., 1988). This de-
72 viation in SWH is characterized as an increase or simply a bump in SWH during late
73 spring and early summer caused by expansion fans that generate locally forced waves
74 that dominate the wave field (Villas Bôas et al., 2017). These wind events have been hy-
75 pothesized by winant1988marine to be present in other oceanic regions that have coastal
76 topography and atmospheric conditions similar to California. These regions include the
77 west coast of Australia, the coast of Namibia, the coast of Chile, the southern Caribbean

78 sea, the northwest coast of Africa near Morocco, and in the Arabian sea near the tip of
 79 Somalia. These include eastern boundary current regions, monsoon regions, and regions
 80 significantly sheltered from remotely forced waves. Here, we refer to these regions col-
 81 lectively as summer wind anomaly regions (SWARs). To our knowledge, there has been
 82 no exploration of the possible influence of regional-scale wind variability on the intraan-
 83 nual variability of SWH in these SWARs. This is the objective of our paper.

84 In this study we assess whether the seasonality seen in the California Current is
 85 typical of SWARs in other regions, characterized by local effects that are out of sync with
 86 high-latitude winter storms. Global-scale satellite observations from 1993 to 2015 are used
 87 to identify the timing of the WSP seasonal cycle and to evaluate whether this aligns with
 88 the SWH seasonal cycle. This can lead to a deeper understanding of the wave climate
 89 and the sea-state in these partially wind-sea dominated regions. Additionally, this study
 90 gives possible expectations for sea-state dependent air-sea fluxes (?, ?) while also pro-
 91 viding quantitatively approach for identify SWARs. Practical applications include man-
 92 aging coastal and oceanic resources such as coastal shipping and navigation within SWARs
 93 (Stopa, 2019).

94 This paper is organized as follows. Section 2 describes the data sets used to ana-
 95 lyze global SWH and the limitations of our analysis. Section 3 explores the parameters
 96 of the annual and semi-annual SWH and WSP models globally as well as regional cli-
 97 matologies. Section 4 uses wave age to illustrate that SWH measurements during the spring
 98 and summer months within SWARs are observing wave fields dominated by locally forced
 99 waves rather than remotely forced waves justifying the claim that local wind events cause
 100 the deviation from the seasonal cycle. Section 5 summarizes our conclusions.

101 **2 Methods**

102 **2.1 Remotely sensed Data**

103 Wave data used in this study are drawn from over two decades (1 January 1993
 104 to 31 December 2015) of cross-calibrated satellite altimeter SWH measurements produced
 105 by the Institut français de recherche pour l'exploitation de la mer (Ifremer) (Queffeulou
 106 & Croizé-Fillon, 2017). Ifremer's SWH altimeter dataset combines cross-calibrated mea-
 107 surements from multiple near-pole non-sun synchronous satellites which are also calibrated
 108 against buoy observations. Here, we binned the daily along track data onto a 1° by 1°

109 spatial grid. Satellites incorporated in this Ifremer product include ERS-1&2, TOPEX-
 110 Poseidon, GEOSAT Follow-ON (GFO), Jason-1, Jason-2, ENVISAT, Cryosat and SARAL
 111 AltiKa [for more details see][]Queffeulou2017Global.

112 Sea surface wind data for this study are from the Cross Calibrated Multi-Platform
 113 version 2 (CCMP2) wind vector analysis produced by Remote Sensing Systems (Atlas
 114 et al., 2011). CCMP2's data product is released on a 0.25° by 0.25° spatial grid with 6
 115 hourly temporal resolution. For this analysis, we averaged CCMP2 winds spatially to
 116 a 1° by 1° grid and temporally to daily resolution in order to match the Ifremer grid-
 117 ded SWH data. The CCMP2 product incorporates measurements from scatterometers,
 118 radiometers, in situ buoys, and modelled wind velocity data (Atlas et al., 2011). CCMP2
 119 provides zonal and meridional components of winds 10 meters above the sea surface (Atlas
 120 et al., 2011), which are used to compute WSP.

121 The Ifremer SWH product is typically offset in time by about 6 hours relative to
 122 the CCMP2 wind product. For point-to-point analysis, this would present a major ob-
 123 stacle due to the fact that SWH and WSP are highly variable on time scales of minutes
 124 to hours and can change significantly within a 6 hour period. Since the data are not suited
 125 for analysis of the instantaneous response of SWH to WSP, the analysis done in this study
 126 focuses on longer time scales, using monthly averaged SWH and WSP.

127 **2.2 Monthly Climatology: Annual and Semi-Annual Variability**

128 In order to analyze the annual and semi-annual variability of SWH and WSP at
 129 each grid point, we apply a least-squares fit to SWH and WSP with five parameters to
 130 represent the mean, annual, and semi-annual sinusoidal cycles.

131 The linear trend in the SWH and WSP time series was removed from the WSP and
 132 SWH monthly data before computing the model and its parameters. The magnitude of
 133 the linear trend was obtained by computing a least-squares fit accounting for a linear
 134 trend and inspecting the coefficient of the linear term. For SWH and WSP, the linear
 135 trend magnitude is two orders of magnitude smaller than the annual and semi-annual
 136 temporal variability. Consequently, it is removed for completeness.

137 The parameters used to evaluate and compare the annual and semi-annual cycles
 138 spatially were the amplitude and phase constant. Amplitude and phase constant are com-

139 puted individually for the annual and semi-annual cycle of SWH and WSP. In order to
 140 evaluate the percent of variance explained by the model, the coefficient of determination
 141 is used.

142 For the climatological analysis within SWARs, SWH and WSP grid points inside
 143 4° by 4° square regions were first temporally averaged into monthly averages and then
 144 spatially averaged in order to obtain SWH and WSP monthly climatologies for each SWAR.
 145 The 4° by 4° regions were picked by looking at seasonally averaged WSP maps within
 146 SWARs. We chose 4° by 4° regions that had anomalously high WSP and small spatial
 147 WSP gradients, as seen in Figs. 6 and 7. The seasonal average from boreal summer was
 148 used in the Northern Hemisphere and austral summer in the Southern Hemisphere in
 149 order to illustrate high WSP present in SWARs.

150 Seasonal maps of December-January-February (DJF) and June-July-August (JJA)
 151 for the mean and standard deviation of SWH and WSP illustrate the seasonal evolution
 152 and variance of the data (Fig 1).

153 2.3 Limitations of Data

154 The data used in this study have limitations originating from Ifremer and CCMP2
 155 data product admonitions, the use of integral parameters instead of spectral data, and
 156 land contamination. Ifremer's SWH data product has been validated by queffeulou2004long
 157 by comparing SWH measurements with in situ buoy observations and ensuring near ho-
 158 mogeneity of SWH measurements between satellite missions. However, the dynamic range
 159 in the altimeter data is attenuated relative to in situ observations: high altimetric SWH
 160 underestimates in situ SWH, and low altimetric SWH overestimates in situ SWH (Queffeulou,
 161 2004), with the high steepness of waves in the wave field causing other discrepancies. CCMP2
 162 data has caveats include a possible spurious trend due to ECMWF's assimilation pro-
 163 cess and underestimation of wind speeds in high wind regions due to ECMWF winds'
 164 tendency to underestimate wind speed (Atlas et al., 2011). The annual and semi-annual
 165 cycles are stronger signals present in the WSP climate in SWARs and would therefore
 166 not be as affected by spurious trends. However, underestimation of WSP could affect the
 167 analysis of SWARs which are high wind regions during summer months. Integral param-
 168 eters are used in this analysis with the understanding that they have limited skill in de-
 169 scribing all systems present in the wave field. echevarria2019seasonal highlight this short-

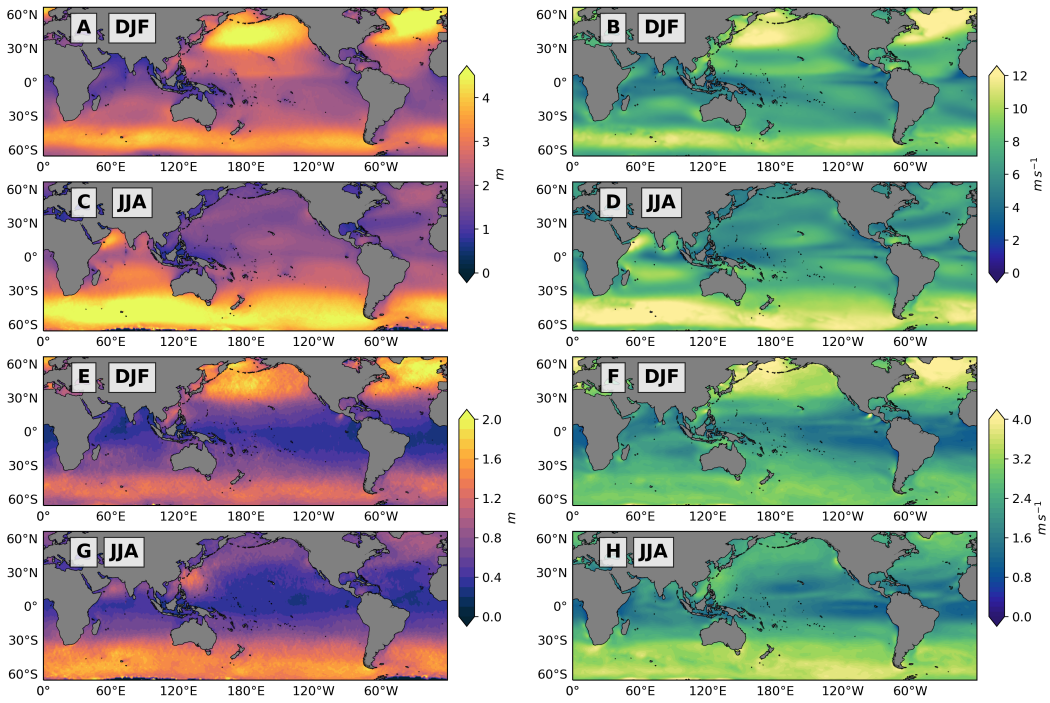


Figure 1. DJF seasonal mean for (A) Ifremer SWH and (B) CCMP2 WSP; JJA seasonal mean for (C) Ifremer SWH and (D) CCMP2 WSP; DJF seasonal standard deviation for (E) Ifremer SWH and (F) CCMP2 WSP; JJA seasonal standard deviation for (G) Ifremer SWH and (H) CCMP2 WSP. See text for details of computation.

coming of integral parameters in wave climatology analysis and present a climatological analysis of directional wave spectra via principal component analysis of the spectral data from WaveWatch III ECMWF reanalysis data. semedo2011global also used WaveWatch III ECMWF reanalysis data in order to analyze the global wave climate by partitioning 2D wave energy spectrum at each grid point into wind-sea and swell frequency bands and computing integral parameters such as SWH for these partitions.

Lastly, satellite altimetry data $O(10\text{-}100)$ km from shore should be excluded from the analysis due to the data being possibly contaminated by land. Fortunately, local wind anomalies extend several hundreds of kilometer off shore (Winant et al., 1988), allowing reliable SWH and WSP data satellite data to be recorded.

180 3 SWH and WSP Annual and Semi-annual Variability Analysis

181 3.1 Global parameters of Annual and Semi-annual Model and Implica- 182 tions to SWARs

183 To give additional motivation for exploring SWARs, the coefficient of determina-
184 tion can be employed. Coefficient of determination global maps (Fig. 2A,B) assess the
185 percentage of the variability explained by the annual and semi-annual cycle for SWH and
186 WSP respectively. Features in the coefficient of determination maps for SWH and WSP
187 align with features in the SWH and WSP annual and semi-annual amplitude maps (Fig. 3
188): the percent of variation explained by the model is highest in regions with high am-
189 plitude and lowest in region of near zero amplitude. For SWH in SWARs (Fig. 2), the
190 percentage of variability explained typically ranges from 10% to 40%. The Arabian Sea
191 ($5\text{--}21^{\circ}\text{N}$, and $51\text{--}71^{\circ}\text{E}$) is an exception, with nearly 100% of variability explained by
192 annual and semi-annual cycles. In most SWARs, the annual and semi-annual cycles ex-
193 plain only a small fraction of the variability because of the low amplitude annual and
194 semi-annual cycles in these regions. Low percentages can indicate other forcing mech-
195 anisms at work in these regions which contribute more significantly to the wave field. One
196 of these forcing mechanisms for the wave field is the deviation from the seasonal cycle
197 from local wind events.

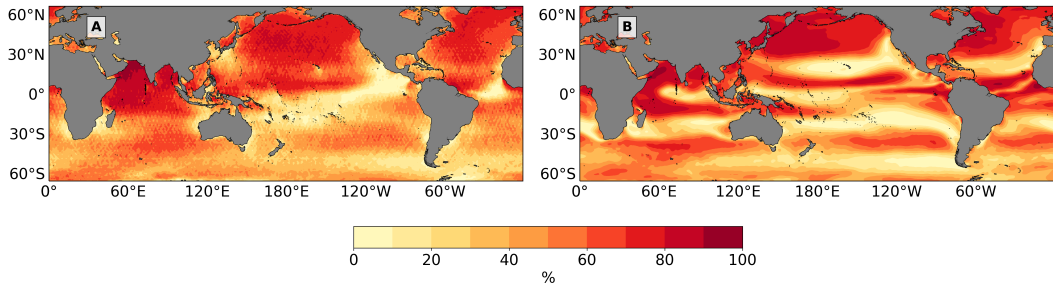


Figure 2. Global map of coefficient of determination for Ifremer SWH (A) and CCMP2 WSP (B) using unweighted annual and semi-annual least squares fit from January 1st, 1993 to December 31st, 2015 for a metric of the goodness of fit of the model.

198 We begin with a global perspective of the SWH and WSP annual and semi-annual
199 cycle parameters to identity and locate SWARs and then focus regionally to gain a deeper
200 understanding of the relation between the wind and wave climate. Figure 3 compares

201 the Ifremer SWH annual and semi-annual cycle amplitude and phase with CCMP2 WSP
 202 parameters. Notice that the phase has been converted from radians to months.

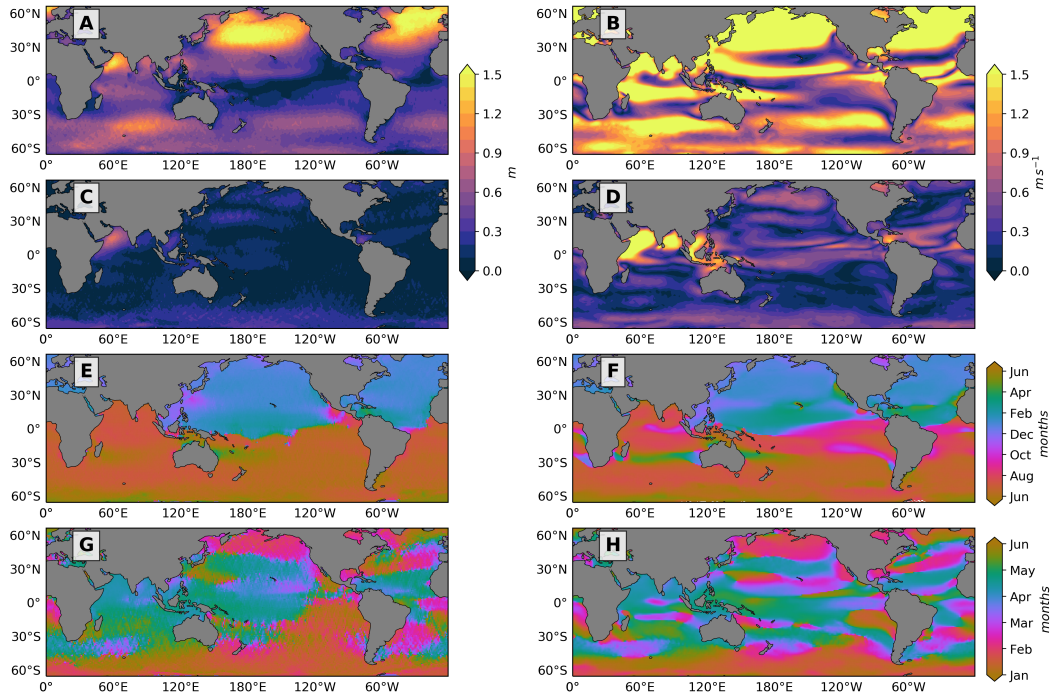


Figure 3. Amplitude of annual cycle for (A) Ifremer SWH and (B) CCMP2 WSP; amplitude of semi-annual cycle for (C) Ifremer SWH and (D) CCMP2 WSP; phase of annual cycle for (E) Ifremer SWH and (F) CCMP2 WSP; phase of semi-annual cycle for (G) Ifremer SWH and (H) CCMP2 WSP. See text for details of computation.

203 The annual cycle amplitude of both SWH and WSP (Fig. 3A,B) is largest in the
 204 high latitudes of the Northern Hemisphere but smaller in the high-latitude Southern Hemisphere.
 205 This implies that SWH and WSP in the Northern Hemisphere generally experiences more seasonal variability than in the Southern Hemisphere where mean SWH and
 206 WSP are much more consistently high (Fig. 1A-D). For SWH, high-amplitude annual
 207 cycles also occur in the Arabian Sea and in a zonal bands from 30° - 45° in the Northern and Southern Hemispheres. In the tropical Pacific and Atlantic, the amplitude drops
 208 to near zero. This near-zero region is not located directly on the equator, and its latitude varies with longitudinal position. For WSP, there are many interesting high amplitude features in the Indian Ocean and the equatorial Pacific and Atlantic. Similar high
 209
 210
 211
 212

213 amplitude regions in the Indian and Southern Ocean are seen for SWH. In contrast to
214 SWH, the WSP amplitude does not tend towards zero near the equator.

215 The semi-annual cycle of SWH and WSP is smaller in amplitude than the annual
216 cycle (Fig. 3C,D). The highest amplitude semi-annual cycles for both WSP and SWH
217 occur in the Arabian Sea and Southern Caribbean, while the Bay of Bengal and the South
218 China Sea have high amplitude only for WSP. These regions are a collection of monsoon
219 regions and SWARs.

220 The annual cycle phase map for SWH and WSP (Fig. 3E,F) generally shows that
221 the Northern Hemisphere is approximately 6 months out of phase with the Southern Hemi-
222 sphere. In many regions across the globe, the SWH and WSP annual cycles are roughly
223 in phase, implying that maximum wave height coincides in time with maximum WSP.

224 Features in the SWH annual cycle phase map include high spatial variability in the
225 Southern Hemisphere with more localized regions in the Northern Hemisphere. A few
226 patches stand out in Fig. 3E,F in which the month of maximum wind deviates from the
227 predominant hemispheric phasing. Some of these places have a low-amplitude annual cy-
228 cle, which indicates that the phase is not well constrained. For example, in the equato-
229 rial Pacific and Atlantic, a large phase gradient occurs in regions where the amplitude
230 of the seasonal cycle is near zero. Other characteristics of this transitional region include
231 low to moderate seasonally averaged SWH (Fig. 1A,C) with low variance (Fig. 1E,G).
232 This phase boundary designates the transition from the seasonal cycle being primarily
233 set by storm system originating in the Northern Hemisphere to storm systems originat-
234 ing in the Southern Hemisphere. This rapid transition in phase is also known as a swell
235 front (Young, 1999; Semedo et al., 2011; Jiang & Chen, 2013). However, waves propa-
236 gating from the Northern and Southern Hemispheres coexist superimposed on the wave
237 field at and beyond the swell front (Echevarria et al., 2019). This means that the waves
238 from each hemisphere propagate in opposing directions.

239 At the swell front in the equatorial Pacific (enlarged in Figure 4), several abrupt
240 shifts in phase exist between 10° and 20°S at approximately 180°E and 145°W. One ex-
241 planation for these abrupt phase shifts is island shadowing. Waves from the Southern
242 Ocean propagating northward encounter the topography of Polynesian islands causing
243 the waves to break and dissipate on the south-facing coastlines. As a result, to the south

244 of the islands, waves follow the Southern Hemisphere seasonal cycle, while the ocean to
 245 the north is in phase with the Northern Hemisphere seasonal cycle.

246 Some waves are refracted by the islands. Waves from the Southern Ocean that are
 247 able to propagate through the Polynesian islands continue toward the northern Pacific.
 248 For example, at approximately 170°W and 145°W (Figure 4A), regions with, June-August
 249 maxima (i.e. Southern Hemisphere dominated wave fields) occur north of regions of December-
 250 February maxima (i.e. Northern Hemisphere dominated wave fields).

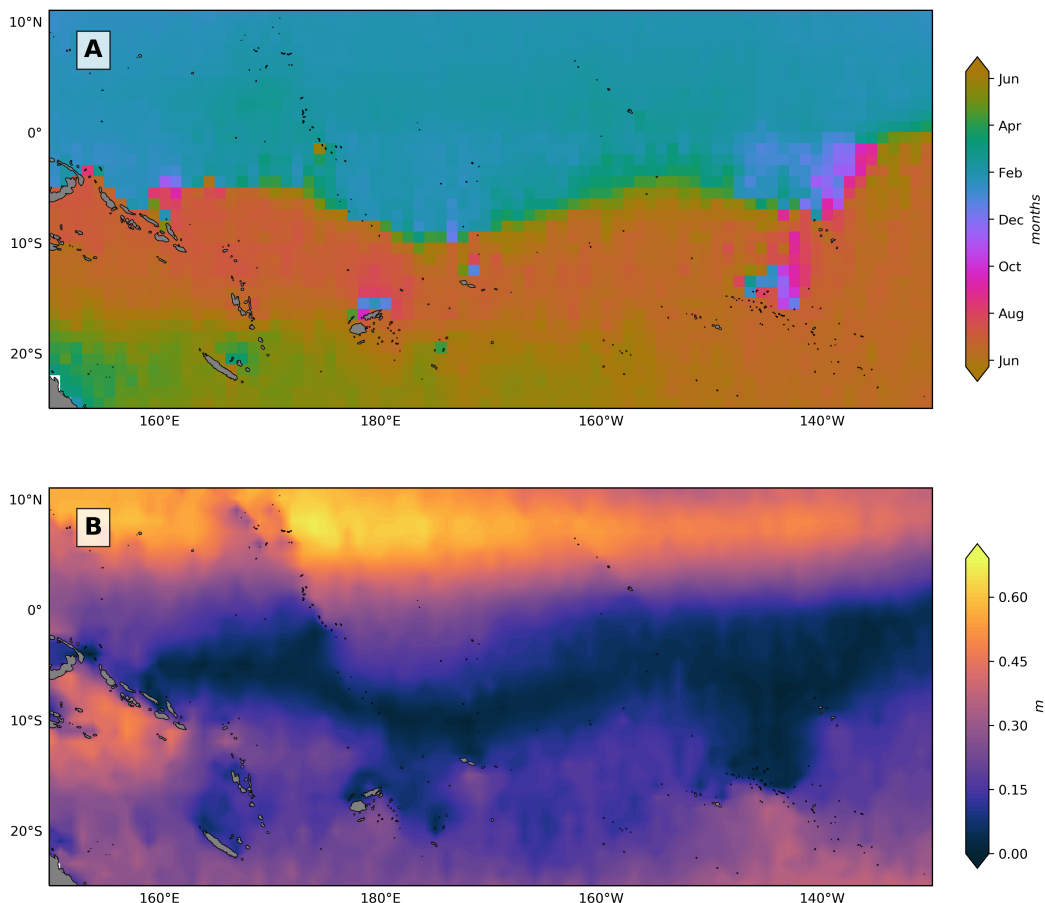


Figure 4. (A) Ifremer SWH Annual cycle phase map in Polynesian island region illustrating island shadowing, (B) Ifremer SWH annual cycle amplitude map in Polynesian island region

251 The location of the swell front in the Pacific and Atlantic does not lie along the equator.
 252 The Pacific swell front is slightly south of the equator between 5° and 10°S in the
 253 western Pacific starting at 170°W , and shifts equatorward further east (Figure 4A). The
 254 Atlantic swell front aligns closely with the equator in the western Atlantic and abruptly

shifts north of the equator near the western coast of Africa. Both swell fronts in the Pacific and Atlantic occur in near zero SWH annual cycle amplitude regions. Explanations for the geographic location of these boundaries is beyond the scope of the study and will be left for future research.

SWH and WSP annual cycle phase maps display two important features within SWARs. First, in most SWARs, the annual cycle of WSP is approximately 4 to 6 months out of phase with the expected phase of the WSP set by hemispheric large-scale storm systems. In the California Current SWAR, this phase inconsistency means that instead of seeing a WSP maximum in boreal months, we find the maximum to be shifted by 4 to 6 months to boreal spring or summer. Fig 5A identifies regions where the WSP annual cycle phase corresponds to a maximum occurring during April through August (boreal summer and early spring) in the Northern Hemisphere and a maximum occurring during December through February (austral summer) in the Southern Hemisphere. From Fig 5A, we observe that SWARs are between 4 to 6 months out of phase with the expected hemisphere phase with the exception of the Arabian and South Caribbean Seas. Conditions for being anomalous in the Northern Hemisphere is less restrictive than the Southern Hemisphere because the WSP annual cycle off the California and Moroccan coasts reach a maximum during the early spring rather than during the summer (Fig. 3F). This less restrictive condition in the Northern Hemisphere caused a region across the central Atlantic to be considered anomalous. However, this region has a low amplitude annual cycle, implying small significance. All SWARs have significant high annual cycle amplitudes. Furthermore, marginal seas and the equatorial regions across the Pacific and Atlantic oceans were not considered in Fig 5A.

Second most SWARs are also characterized by a 4 to 6 month phase difference between SWH and WSP annual cycles. In Fig 5B this phase relationship is visible in all SWARs with the exception of the Arabian and South Caribbean Sea. villas2017characterization showed a similar phase relationship results in the California SWAR from SWH and WSP.

Using these two features, we develop a quantitative approach to identify SWARs and to evaluate the effect of local winds on the wave field. If a region has an anomalous WSP annual cycle phase as described above with a sufficiently high amplitude annual cycle, then the region can be considered a SWAR. The candidate SWARs determined by this metric (highlighted in Fig 5A) largely agree with the hypothesized expansion fan

287 wind regions identified by winant1988marine. However, the wind anomalies highlighted
 288 by this approach can be generated by a broad range of atmospheric forcings other than
 289 expansion fan wind events. Furthermore, this approach fails to highlight hypothesized
 290 expansion fan wind regions in the Arabian and South Caribbean Seas.

291 For the effects local winds have on the wave field, the phase relationships between
 292 SWH and WSP indicates that deviations from the SWH annual cycle may occur in SWARs.
 293 Deviations are more likely to be present if the maximum in the WSP annual cycle oc-
 294 curring during the minimum of the SWH annual cycle because locally forced waves have
 295 a higher probability of dominating the wave field over remotely forced waves. Therefore,
 296 due to the phase difference between WSP and SWH being 4 to 6 months, SWARs are
 297 more likely to have deviations from the SWH annual cycle present. However, this de-
 298 pends on local conditions of the wave field during the spring, summer, and fall, which
 299 will be discussed later.

300 To assess the global extent of anomalous local surface winds over the world oceans,
 301 the fraction of the oceans experiencing anomalous winds and phase difference was com-
 302 puted using WSP and SWH annual cycle phase (Fig 5A,B). Using the same categoriza-
 303 tion outlined previously for anomalous WSP phase and excluding marginal seas and the
 304 equatorial regions across the Pacific and Atlantic Oceans from the calculation, we found
 305 that approximately 1.65% of the world oceans have anomalous high WSP during the spring,
 306 summer, and fall months. When computing these percentages, the amplitude of the an-
 307 nual cycle was also considered: regions with an annual cycle amplitude less than 0.25 m
 308 were not considered. This calculation is approximate and not highly rigorous. However,
 309 it gives a general impression of the extent and geographic locations where these anom-
 310 lous winds and phase differences occur.

311 The semi-annual cycle phase map for SWH and WSP (Fig. 3G,H) has more spa-
 312 tial structure. However, due to the generally low amplitude semi-annual cycle amplitude
 313 in all ocean basins, the significance of the spatial variability in the SWH and WSP phase
 314 map's variability is low except for a few regions where the semi-annual amplitude is high.
 315 These regions for SWH and WSP have been mentioned previously.

316 Globally analyzing the wind and wave climate has led to the identification of SWARs
 317 using the SWH and WSP's annual cycle phase. To understand the impact of the phase

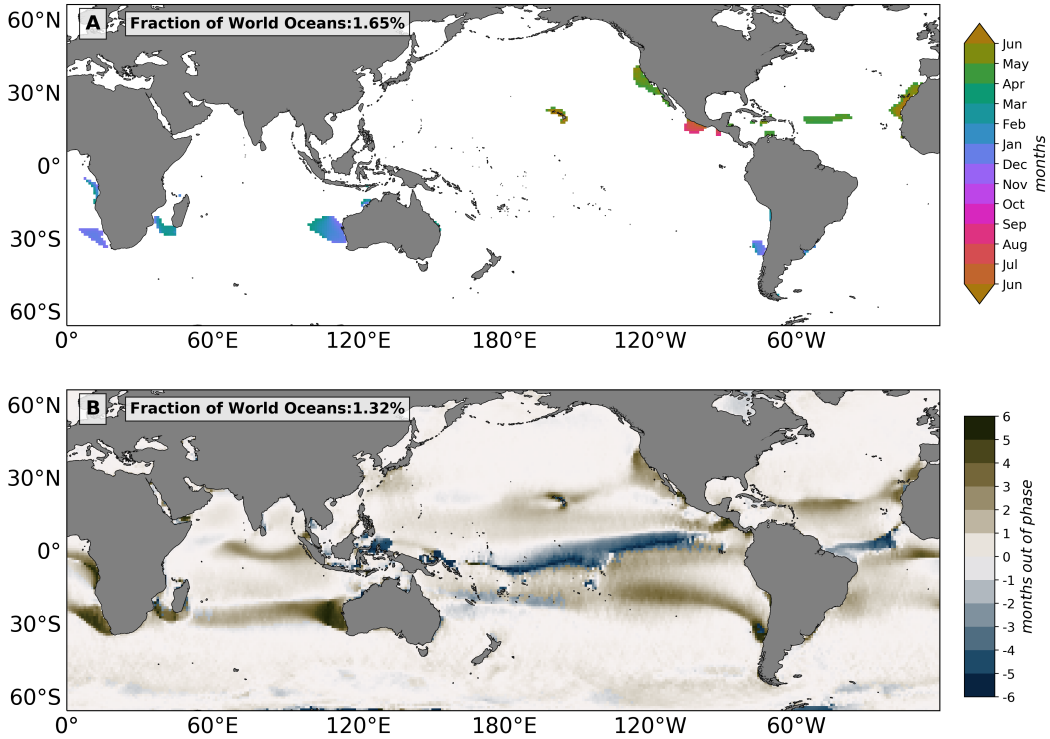


Figure 5. (A) CCMP2 WSP Annual cycle phase map highlighting anomalous WSP phase regions, (B) Annual Cycle phase difference between WSP and SWH with fraction of the world's oceans that experience anomalous local surface winds and phase difference respectively. See text for details on categorization of anomalous WSP phase and phase difference.

relationship between SWH and WSP within SWARs regional on the wave field, a regional monthly climatological analysis must be performed.

3.2 Regional Climatologies of SWARs

In order examine how phasing differences in the SWH and WSP annual cycles influence wave fields with SWARs, monthly climatologies for SWH and WSP were computed from January 1st, 1993 to December 31st, 2015 within 4° by 4° grid boxes. Figs. 6 and 7 show the regional climatologies from SWARs in the Northern and Southern Hemispheres respectively as well as the 4° by 4° regions within each SWAR where the climatology is computed. The standard error of the mean (shading in panes on the right) was computed using decorrelation time scales calculated from in-situ observations in Northern California and Southern Caribbean SWARs. Based on similarities in wind and wave climatologies, Northern California decorrelation time scales were applied to Western Aus-

330 tralia, North Africa, South Africa, and Central-West South America while Southern Caribbean
 331 decorrelation time scales were applied to the Arabian Sea. The climatologies show a clear
 332 difference between Northern and Southern Hemisphere SWARs and between eastern bound-
 333 ary current regions and monsoon or tropical storm regions with respect to the influence
 334 the phase relationship between wind and wave fields.

335 The two hemispheres are distinctly different. In all Northern Hemisphere SWARs,
 336 the maximum in the WSP climatology is concurrent with a deviation from the sinusoidal
 337 SWH annual cycle. Examples include the Northern California and North African SWARs
 338 (Fig. 7B,F). Off the coast of California, the WSP seasonal cycle reaches a maximum in
 339 June, simultaneous with an increase in SWH. In the North African region, a WSP max-
 340 imum and a deviation from the SWH seasonal cycle occur in July. In both cases, the ob-
 341 served seasonal maxima deviated by more than one standard error from the fitted sea-
 342 sonal cycle. In contrast, in the Southern Hemisphere, the maximum in the WSP causes
 343 a small or near zero magnitude deviation from the SWH annual cycle, for example, in
 344 February off the coast of western Australia (Fig. 7B). Off the coasts of Chile and Namibia
 345 (Fig. 7D,F), deviations from the seasonal cycle are not present at all in the SWH clima-
 346 tology. Therefore, we hypothesize that in Southern Hemisphere SWARs (Fig. 7), local
 347 winds have comparatively less influence on the wave climate than in the Northern Hem-
 348 isphere. This is presumed to occur because the magnitude of the deviation in the SWH
 349 cycle is determined by the local conditions and characteristics of the wave field within
 350 the region. Local conditions refers to the exposure and distance of the SWAR from re-
 351 motely forced waves generation regions. In other words, how sheltered the SWAR is to
 352 regions with storms that produce remotely forced waves with high SWH.

353 Off the coast of Western Australia, the increase in the SWH climatology during aus-
 354 tral summer has small magnitude due to this SWAR's high exposure to the Southern Ocean
 355 where large storms produce large amplitude remotely forced waves. These remotely forced
 356 waves propagate into the Western Australian SWAR and overwhelm the wave field caus-
 357 ing the locally forced waves to be significantly less likely to dominate the wave field. There-
 358 fore, the wave field is primarily dominated by the remotely forced waves throughout the
 359 year with a small exception in January when locally forced waves dominate the wave field.
 360 For the other two SWARs in the Southern Hemisphere, the wave field tends to be dom-
 361 inated by remotely forced waves year round.

The monsoon region in the Arabian Sea and the tropical storm region in the southern Caribbean Sea differ from eastern boundary currents in their wind and wave climates. In the Southern Caribbean Sea, the SWH climatology is in phase with the WSP climatology (Fig 6D). This implies that local wind events, including the SWA, generate the waves within the region. This can be explained by the fact that the Southern Caribbean SWAR is protected by Antilles Islands and has little exposure to waves propagating from high latitudes (Semedo et al., 2011) (Fig 6C). The increases in SWH and WSP during boreal summer cause two maxima per year in the wind and wave climates which explains the large amplitude semi-annual cycle for SWH and WSP (Fig 3C,D). A similar semi-annual pattern occurs in the Arabian sea, where monsoon winds generate high locally forced waves, with the wave field dominated by locally forced waves. However, this SWAR is not sheltered from remotely forced waves that propagate northward from the Southern Ocean.

4 Wind-sea vs. Swell Dominance in SWARs

4.1 Local vs. Remotely Forced Waves

In order to evaluate whether these deviations from the SWH annual cycle are produced by local wind events or remote storms, characteristics of locally and remotely forced waves must be established. During a storm, wind blows over a length of ocean surface called fetch at certain speed and for a given time duration, generates waves (Ardhuin, 2015). While the atmosphere is still supplying energy to the wave field causing the frequency spectrum to evolve, the waves are categorized as locally forced waves or wind-seas. These waves tend to be high frequency, high amplitude, and steep, leading to dissipation over relatively short distances (Ardhuin et al., 2009). Once the wind is no longer inputting energy and momentum into the waves, the waves are categorized as remotely forced waves or swell. Swell tends to be low frequency and propagates long distances dispersively, with low-frequency waves at higher phase speeds than high-frequency waves (Snodgrass et al., 1966).

Wave age provides an empirical metric to distinguish between wind-sea and swell waves. It quantifies the stage of development of waves (Alves et al., 2003). The wave age criterion is defined as

$$\text{Wave Age} = \frac{C_p}{U_{10}}, \quad (1)$$

392 where C_p is the phase speed at the peak of the spectrum, and U_{10} is the wind speed 10 m
 393 elevation. Here,

$$\frac{C_p}{U_{10}} > 1.2 \quad \text{Remotely Forced Waves} \quad (2)$$

$$\frac{C_p}{U_{10}} \leq 1.2 \quad \text{Locally Forced Waves.} \quad (3)$$

394 This criterion is based on the finding that wave growth stops, or at least slows, when wave
 395 age is greater than 1.2 (Donelan et al., 1992). This corresponds with waves crests trav-
 396elling 20% faster than the wind speed 10 meters above the ocean surface, so that the waves
 397 are outrunning the wind and not able to receive further wind energy input. We assume
 398 that the satellite observes deep water waves, with a wavelength much less than the wa-
 399 ter depth. For deep water waves with peak frequency f_p , the deep water dispersion re-
 400 lationship yields the peak phase speed:

$$C_p = \frac{g}{2\pi f_p}. \quad (4)$$

401 The wave field can represent a superposition of multiple wave systems. The peak
 402 phase speed represents the phase speed of the most energetic wave system. Thus although
 403 both swell and wind-sea wave systems are likely to co-exist in the wave field, the sep-
 404 aration process categorizes the wave field as being dominated either by swell or by wind-
 405 sea waves. Wave age has deficiencies in the accuracy of this categorization, and more ro-
 406 bust wind-sea and swell separation techniques exist ()�.

407 4.2 Probability of Swell: Wave Age Method

408 Using wave age, probability of swell can be obtained to illustrate the fraction of
 409 time the wave field is swell-dominated relative to the total number of wave events:

$$\text{Probability of swell} = \frac{N_{swell}}{N_{total}} \quad (5)$$

410 where N_{swell} is the number of observations with wave age exceeding 1.2 representing a
 411 swell-dominated wave field and N_{total} is the total number of observations in the time se-
 412 ries.

413 Probability of swell has previously been computed globally by jiang2013global and
 414 by semedo2011global, both of whom showed that remotely forced waves dominate the
 415 wave field in all ocean basins with the exception the Southern Ocean, some coastal re-

416 gions and common storm tracks (Jiang & Chen, 2013; Semedo et al., 2011), where wind-
 417 generated waves play a stronger role.

418 Probability of swell in SWARs can confirm if the wave fields observed during the
 419 late spring and summer months are dominated by wind seas or by swell propagating from
 420 distant storms.

421 Altimeters provide access to SWH with no information on wave frequency and di-
 422 rection (Chelton et al., 2001). Therefore, to calculate phase speed of waves and conse-
 423 quently wave age, we use WaveWatch 3 (WW3) modeled data with peak frequency. Cli-
 424 mate Forecast System Reanalysis (CFSR) winds provided the forcing to WW3 wave model
 425 in order to obtain peak frequency with 6 hourly temporal and 0.5 degree spatial reso-
 426 lution. Wave age was computed after decreasing the spatial resolution of WW3 peak fre-
 427 quency and CFSR WSP to 1 degree and the temporal resolution to daily time steps. The
 428 WW3 and CFSR products were used instead of the coupled ECMWF wind product and
 429 WW3 wave parameters because CFSR WSP forcing WW3 SWH has more seasonal vari-
 430 ability, and prediction accuracy has improved in recent years (Stopa & Cheung, 2014).
 431 However, the WW3 and CFSR data sets have potential biases, including overestimation
 432 of SWH and WSP as compared to in situ buoy observations and less temporal homo-
 433 geneity than the ECMWF-forced WW3 model (Stopa & Cheung, 2014). This allows CFSR
 434 and WW3 to more accurately model extreme weather events (Stopa & Cheung, 2014).

435 Before computing wave age, the performance of CFSR WSP and WW3 peak fre-
 436 quency are examined. Regional climatologies of WW3 SWH and CFSR WSP data are
 437 computed, using the same method used for Figs. 6 and 7. Fig 8 displays regional clima-
 438 tologies of WW3 SWH and CFSR WSP data compared with Ifremer SWH and CCMP2
 439 WSP. Fig 8 shows generally strong agreement in all of the SWARs, indicating the pres-
 440 ence of seasonal wind anomalies. The annual and semi-annual cycles were fitted to WW3
 441 SWH and CFSR WSP. Fitted parameters from WW3 largely agree with altimeter-derived
 442 fitted parameters.

443 Performance assessments of WW3 peak frequency have been studied in the Pacific
 444 basin by hanson2009pacific for the year 2000 using NRAQ+ wind fields. Even though
 445 this is not the same winds used in this study, NRAQ+ are a realistic wind forcing. han-
 446 son2009pacific concluded that wave period agrees well with in situ observations. Other
 447 ocean basins have yet to be validated for peak frequency. With the caveat that peak fre-

448 quency has not been validated in other ocean basins because wave buoys are not avail-
 449 able, we will use the WW3 peak frequency.

450 Given the biases in the pdf of WSP and peak frequency from models, wave age may
 451 be biased high or low. Therefore, we recognize that errors between model and remote
 452 observations and uncertainties of the computed wave age exist.

453 Figure 9 shows the seasonal progression of probability of swell. In SWARs the wave
 454 field is dominated by wind seas a high percentage of time, typically during the late spring
 455 and early summer months (Figure 9A,C), when the probability of swell is significantly
 456 lower. For the Northern Hemisphere, off the coasts of California and North Africa, the
 457 probability of swell drops to between 80%–90% in spring and below 75% in summer. Both
 458 the Caribbean and Arabian Seas are consistently below 75% through the entire year, im-
 459 plying that the wave field is always experiences stronger local wave effects than most re-
 460 gions. For the Southern Hemisphere, the probability of swell in the SWARs of West Aus-
 461 tralia, Chile, and Namibia ranges from 90% to 95%, which is not as low as in Northern
 462 Hemisphere SWARs. These results are consistent with the hypothesis that the devia-
 463 tion from the SWH annual cycle results from comparatively more locally forced waves.
 464 The results also support the hypothesis that compared with the Northern Hemisphere
 465 SWARs, Southern Hemisphere SWARs are less dominated by locally forced waves be-
 466 cause their swell waves originate from the Southern Ocean, which generates strong swell
 467 with a weak annual cycle.

468 Figure 9 is consistent with probability of swell maps produced by semedo2011global.
 469 semedo2011global separated wave energy spectra from ERA-40 into wind-sea and swell
 470 partitions using WAM separation frequencies and then computed SWH for each parti-
 471 tion. In seasonal average maps SWARs show increased SWH for the wind sea partition
 472 (Figures 2c and 3c), during JJA in the Northern Hemisphere and during DJF in the South-
 473 ern Hemisphere, consistent with the wave-age-driven probability of swell. This shows con-
 474 sistency between two metrics for evaluating presence and impact of locally forced waves
 475 in SWARs.

476 5 Conclusion

477 We have investigated the wind and wave climates within SWARs to explore whether
 478 the characteristic features of the wind and wave fields observed off the California coast

by villas2017characterization are present in other expansion fan wind regions (Winant et al., 1988). We found that SWARs share anomalous annual cycle phasing for WSP corresponding to late spring or early summer maxima in the WSP annual cycle and 6 month phase difference between WSP and SWH annual cycles. Deviations from the SWH seasonal cycle are high in magnitude in the Northern Hemisphere but have low to near-zero magnitude in the Southern Hemisphere. Monsoon or tropical storm SWARs have concurrence between SWH and WSP climatologies, indicating the wave climate is set by the local wind climate. The fraction of wave variability attributed to local wind events varies depending on local conditions, suggesting that the wave climate in regions that are hypothesized to have expansion fan winds may display variability similar to variability in the Northern California SWAR. In total, 1.64% of the world oceans experience anomalous WSP seasonal variability, illustrating the global extent of these summer wind anomaly events. Low probability of swell in SWARs are observed during the spring and summer months of each hemisphere, along with an increase in the wind-sea component of SWH (Semedo et al., 2011). This implies that there is an increase in the fraction of time that the wave field is dominated by wind-seas and an increase in SWH attributed to these locally forced waves, which supports the hypothesis that the deviation from the SWH annual cycle results from waves that are forced by local wind events.

This improved understanding of the SWH response to local wind events has the potential to lead to more accurate model representations of the wave climate in SWARs. Through understanding the wave climate in these regions, we gain greater insight into the mechanisms by which locally forced wind waves dominate the wave field. When the wave field is dominated by locally forced waves, strong interactions between waves and the atmospheric planetary boundary layer occur (Cavaleri et al., 2012) because wind-forced waves are steep and high frequency. Processes associated with locally forced waves that amplify air-sea interactions include wave breaking and white capping. Both of these processes lead to an increase in heat and mass fluxes by ejecting sea spray into the atmospheric boundary layer, injecting bubbles into the ocean and inducing mixing in the upper ocean (Cavaleri et al., 2012). Sea-state dependent surface wave modulated fluxes of momentum, energy, heat and mass are all essential for climate models to close budgets in the coupled ocean-atmosphere system (Cavaleri et al., 2012). Understanding these fluxes begins with knowing the large scale temporally and spatially varying tendencies of the

511 sea-state of the ocean. Through this study, identification of SWARs with high tendency
 512 for wind-sea dominated wave fields during the spring and summer months are established.

513 **Acknowledgments**

514 This work was supported by the NASA SWOT and Ocean Vector Winds Science Teams,
 515 by a NASA Earth and Space Science Fellowship awarded to Ana Villas Bôas, and by the
 516 Hiestand Scholars program. CCMP Version-2.0 vector wind analyses are produced by
 517 Remote Sensing Systems. Data are available at www.remss.com. We thank the French
 518 Research Institute for Exploitation of the Sea (IFREMER) for providing the satellite al-
 519 timetry significant wave height data (<ftp://ftp.ifremer.fr/ifremer/cersat/products/swath/altimeters/waves>)
 520 and WaveWatch 3 hindcast (<ftp://ftp.ifremer.fr/ifremer/ww3/HINDCAST>).

521 **References**

- 522 Alves, J. H. G., Banner, M. L., & Young, I. R. (2003). Revisiting the pierson–
 523 moskowitz asymptotic limits for fully developed wind waves. *Journal of physi-
 524 cal oceanography*, 33(7), 1301–1323.
- 525 Arduin, F. (2015). *Ocean waves in geosciences*. doi: 10.13140/RG.2.2.16019.78888/
 526 5
- 527 Arduin, F., Chapron, B., & Collard, F. (2009). Observation of swell dissipation
 528 across oceans. *Geophysical Research Letters*, 36(6).
- 529 Atlas, R., Hoffman, R. N., Ardizzone, J., Leidner, S. M., Jusem, J. C., Smith, D. K.,
 530 & Gombos, D. (2011). A cross-calibrated, multiplatform ocean surface wind
 531 velocity product for meteorological and oceanographic applications. *Bull.
 532 Amer. Meteor. Soc.*, 92, 157–174. doi: 10.1175/2010BAMS2946.1
- 533 Cavaleri, L., Fox-Kemper, B., & Hemer, M. (2012). Wind waves in the coupled cli-
 534 mate system. *Bulletin of the American Meteorological Society*, 93(11), 1651–
 535 1661.
- 536 Chelton, D. B., Ries, J. C., Haines, B. J., Fu, L.-L., & Callahan, P. S. (2001). Satel-
 537 lite altimetry. In *International geophysics* (Vol. 69, pp. 1–ii). Elsevier.
- 538 Donelan, M., Skafel, M., Gruber, H., Liu, P., Schwab, D., & Venkatesh, S. (1992).
 539 On the growth rate of wind-generated waves. *Atmosphere-Ocean*, 30(3), 457–
 540 478.
- 541 Echevarria, E. R., Hemer, M. A., & Holbrook, N. J. (2019). Seasonal variability

- 542 of the global spectral wind wave climate. *Journal of Geophysical Research: Oceans*, 124(4), 2924–2939.
- 543
- 544 Jiang, H., & Chen, G. (2013). A global view on the swell and wind sea climate by
545 the jason-1 mission: a revisit. *Journal of Atmospheric and Oceanic Technology*,
546 30(8), 1833–1841.
- 547 Queffeulou, P. (2004). Long-term validation of wave height measurements from al-
548 timeters. *Marine Geodesy*, 27(3-4), 495–510.
- 549 Queffeulou, P., & Croizé-Fillon, D. (2017). *Global altimeter swh data set* (Vol. 2;
550 Tech. Rep.). ZI de la pointe du diable, CS10070, 29280 Plouzan, France:
551 IFREMER.
- 552 Semedo, A., Sušelj, K., Rutgersson, A., & Sterl, A. (2011). A global view on the
553 wind sea and swell climate and variability from era-40. *Journal of Climate*,
554 24(5), 1461–1479.
- 555 Snodgrass, F. E., Hasselmann, K. F., Miller, G. R., Munk, W. H., & Powers, W. H.
556 (1966). Propagation of ocean swell across the pacific. *Philosophical Trans-
557 actions of the Royal Society of London. Series A, Mathematical and Physical
558 Sciences*, 259(1103), 431–497.
- 559 Stopa, J. E. (2019). Seasonality of wind speeds and wave heights from 30 years of
560 satellite altimetry. *Advances in Space Research*.
- 561 Stopa, J. E., & Cheung, K. F. (2014). Intercomparison of wind and wave data from
562 the ecmwf reanalysis interim and the ncep climate forecast system reanalysis.
563 *Ocean Modelling*, 75, 65–83.
- 564 Villas Bôas, A. B., Gille, S. T., Mazloff, M. R., & Cornuelle, B. D. (2017). Char-
565 acterization of the deep water surface wave variability in the california current
566 region. *Journal of Geophysical Research: Oceans*, 122(11), 8753–8769.
- 567 Winant, C., Dorman, C., Friehe, C., & Beardsley, R. (1988). The marine layer off
568 northern california: An example of supercritical channel flow. *Journal of the
569 Atmospheric Sciences*, 45(23), 3588–3605.
- 570 Young, I. (1999). Seasonal variability of the global ocean wind and wave climate.
571 *International Journal of Climatology: A Journal of the Royal Meteorological
572 Society*, 19(9), 931–950.

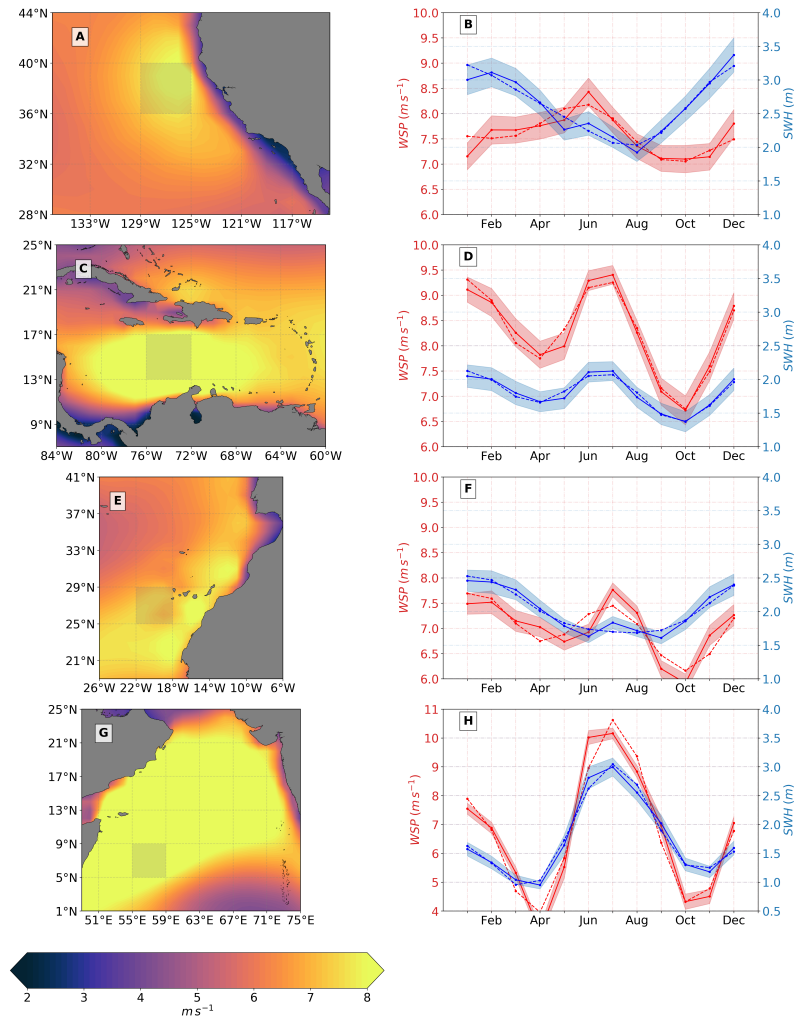


Figure 6. (left column) Northern Hemisphere wind speed in SWARs, averaged over June, July, and August with (right column) Ifremer SWH (solid blue) and CCMP2 WSP (solid red) climatologies extracted from the shaded 4° by 4° boxes within SWARs. Shading represents the standard error of the mean, and dotted blue and red lines are the annual plus semi-annual cycle least-squares fitted to monthly climatology for SWH and WSP respectively. SWARs include Northern California (A and B), Southern Caribbean Sea (C and D), North Africa near the coast of Morocco and western Sahara (E and F), North-Western Arabian Sea (G and H)

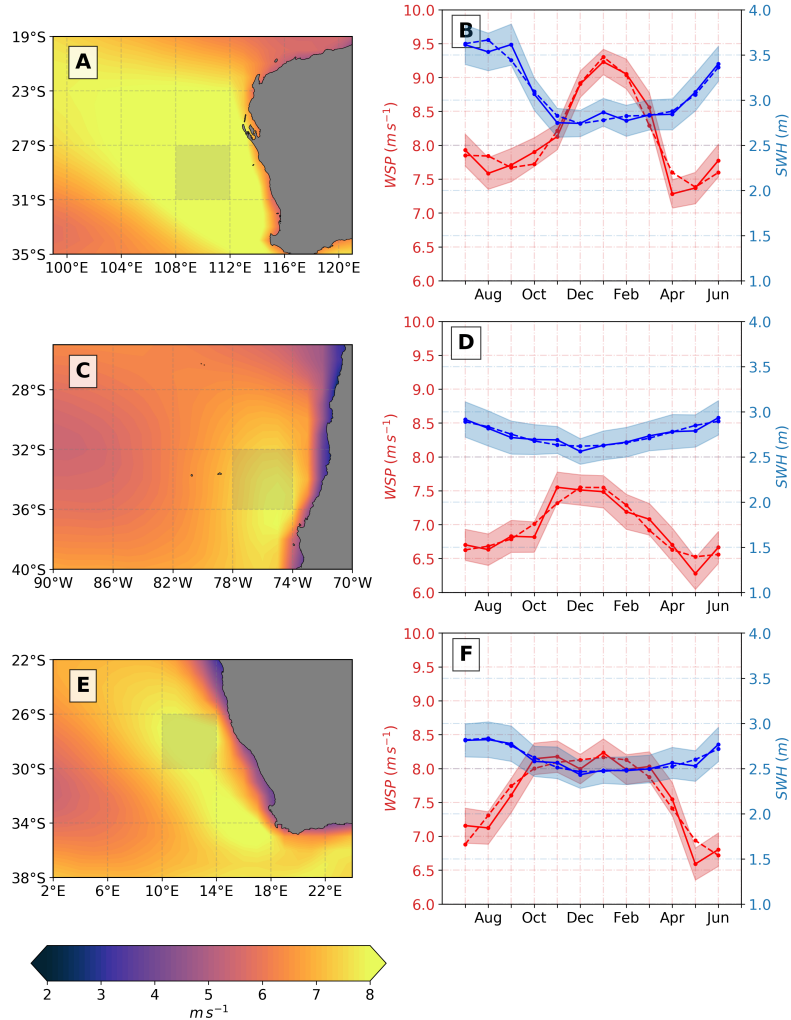


Figure 7. (left column) Southern Hemisphere wind speed in SWARs, averaged December, January, and February with (right column) Ifremer SWH (solid blue) and CCMP2 WSP (solid red) climatologies from the shaded 4° by 4° boxes. Shading and dotted lines are as in Fig. 6. SWARs include Western Australia (A and B), Central Western coast of South America near Chile (C and D), and South-Western Coast of Africa near Namibia (E and F)

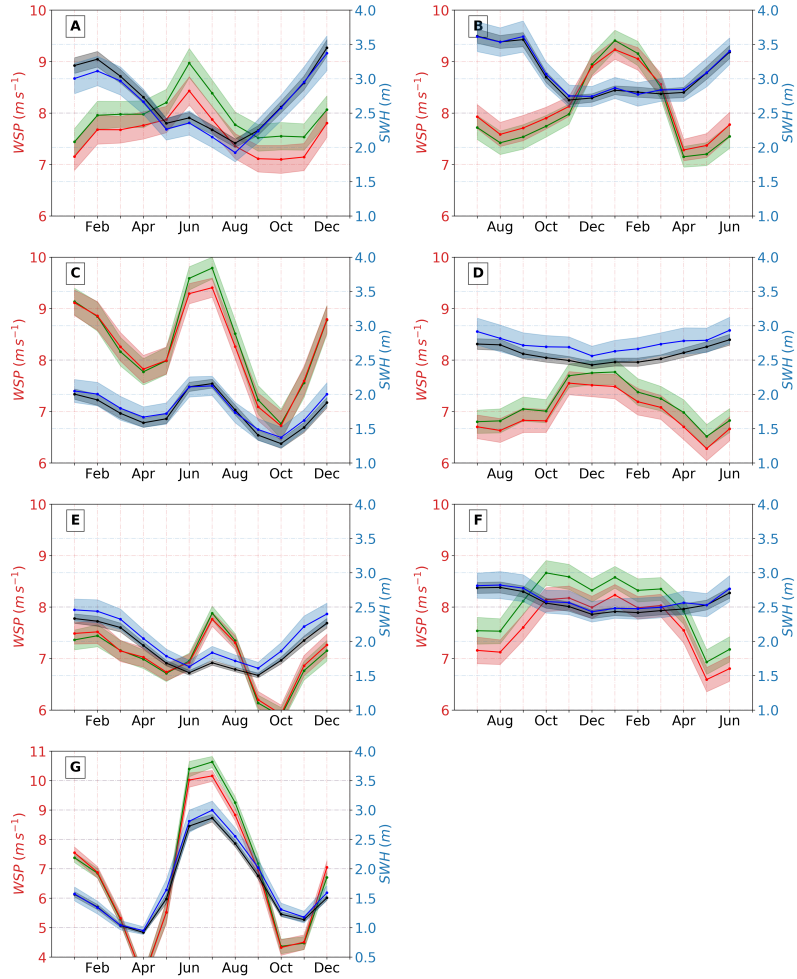


Figure 8. Northern Hemisphere SWARs: (A) North California, (C) Southern Caribbean, (E) North Africa, and (G) Arabian Sea which are the same regions as in Fig 6 and Southern Hemisphere SWARs: (B) West Australia, (D) coast of Chile, and (F) coast of Namibia which are the same regions as in Fig 7

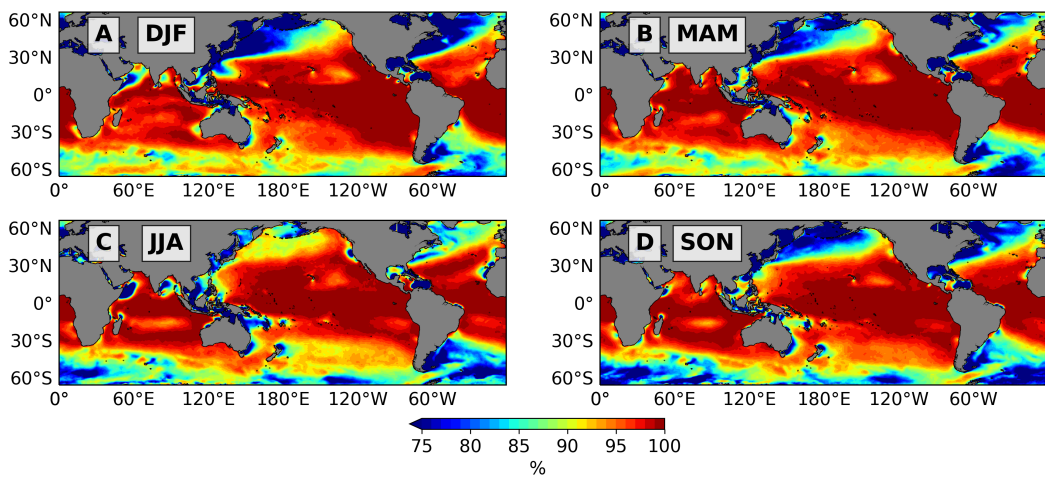


Figure 9. Seasonal progression of probability of swell using wave age criterion and WW3 peak frequency and WSP from January 1st, 1993 to December 31st, 2015 where (A) DJF, (B) MAM, (C) JJA, and (D) SON